Mon. Not. R. Astron. Soc. **000**, 1–15 (2014) Printed 25 December 2014 (MN LATEX style file v2.2)

3D radiative transfer simulations of Eta Carinae's inner colliding winds – I. Ionization structure of helium at apastron

N. Clementel[1⋆], T. I. Madura[2], C. J. H. Kruip[1], J.-P. Paardekooper[3,4] and T. R. Gull[2]
[1]*Leiden Observatory, Leiden University, PO Box 9513, 2300 RA Leiden, the Netherlands*
[2]*Astrophysics Science Division, Code 667, NASA Goddard Space Flight Center, Greenbelt, MD 20771, USA*
[3]*Zentrum für Astronomie, Institut für Theoretische Astrophysik, Universität Heidelberg, Alber–Ueberle–Str. 2, D-69120 Heidelberg, Germany*
[4]*Max Planck Institute for Extraterrestrial Physics, PO Box 1312, Giessenbachstr., D–85741 Garching, Germany*

arXiv:1412.7569v1 [astro-ph.SR] 23 Dec 2014

Accepted 2014 December 8. Received 2014 December 8; in original form 2014 October 2

ABSTRACT
The highly eccentric binary system Eta Carinae (η Car) shows numerous time-variable emission and absorption features. These observational signatures are the result of interactions between the complex three-dimensional (3D) wind–wind collision regions and photoionization by the luminous stars. Specifically, helium presents several interesting spectral features that provide important clues on the geometry and physical properties of the system and the individual stars. We use the SIMPLEX algorithm to post-process 3D smoothed particle hydrodynamics simulation output of the interacting winds in η Car in order to obtain the fractions of ionized helium assuming three different primary star ($\eta_{\rm A}$) mass-loss rates. The resultant ionization maps constrain the regions where helium is singly- and doubly-ionized. We find that reducing $\eta_{\rm A}$'s mass-loss rate ($\dot{M}_{\eta_{\rm A}}$) increases the volume of He^+. Lowering $\dot{M}_{\eta_{\rm A}}$ produces large variations in the volume of He^+ in the pre-shock $\eta_{\rm A}$ wind on the periastron side of the system. Our results show that binary orientations in which apastron is on our side of the system are more consistent with available observations. We suggest that small variations in $\dot{M}_{\eta_{\rm A}}$ might explain the observed increase in He I absorption in recent decades, although numerous questions regarding this scenario remain open. We also propose that the absence of broad He I lines in the spectra of η Car between its 1890's eruption and ~1944 might be explained by $\eta_{\rm B}$'s He^{0+}-ionizing photons not being able to penetrate the wind-wind interaction region, due to a higher $\dot{M}_{\eta_{\rm A}}$ at that time (by a factor $\gtrsim$2, compared to the present value).

Key words: hydrodynamics – radiative transfer – binaries: close – stars: individual: Eta Carinae – stars: mass-loss – stars: winds, outflows

1 INTRODUCTION

Eta Carinae (η Car) is probably most famous for its 'Great Eruption' in the 1840s, when it temporarily became the second brightest non-solar-system object in the sky and ejected ~10–40 $M_\odot$, forming the dusty bipolar 'Homunculus' nebula (Davidson & Humphreys 1997; Smith et al. 2003; Gomez et al. 2010; Steffen et al. 2014). Near the centre of the Homunculus lies η Car itself, an extremely luminous ($L_{\rm Total} \gtrsim 5\times10^6$ $L_\odot$) and highly eccentric ($e \sim 0.9$) binary with a 5.54 yr orbit (Damineli, Conti & Lopes 1997; Hillier et al. 2001; Damineli et al. 2008a,b; Corcoran et al. 2010). The primary component, $\eta_{\rm A}$, is a Luminous Blue Variable (LBV) and our closest example of a supermassive star (D = 2.3 kpc, $M_\star \sim 100\,M_\odot$, $T_{\rm eff} \simeq$ 9400 K; Hillier et al. 2001; Smith 2006). The secondary, $\eta_{\rm B}$, is thought to be a hotter ($T_{\rm eff} \simeq$ 36,000–41,000 K), but less luminous ($L_\star/\,L_\odot \approx 10^5$–$10^6$), O- or Wolf Rayet-type star (Pittard & Corcoran 2002; Verner, Bruhweiler & Gull 2005; Hillier et al. 2006; Teodoro et al. 2008; Mehner et al. 2010).

Because they are so luminous, both components of η Car have powerful radiation-driven stellar winds. Multiwavelength observations obtained over the last two decades (Corcoran 2005; Hamaguchi et al. 2007; Damineli et al. 2008b; Henley et al. 2008; Groh et al. 2010b; Corcoran et al. 2010; Gull et al. 2009, 2011; Teodoro et al. 2013) indicate that $\eta_{\rm A}$'s slow, extremely dense wind ($v_\infty \approx 420\,{\rm km\,s^{-1}}$, $\dot{M}_{\eta_{\rm A}} \approx 8.5\times10^{-4}\,M_\odot\,{\rm yr^{-1}}$; Hillier et al. 2001; Groh et al. 2012a) collides with $\eta_{\rm B}$'s less dense ($\dot{M}_{\eta_{\rm B}} \approx 1.4\times10^{-5}\,M_\odot\,{\rm yr^{-1}}$), but much faster ($v_\infty \approx 3000\,{\rm km\,s^{-1}}$; Pittard & Corcoran 2002; Parkin et al. 2009), wind. This wind–wind collision (WWC) produces the shock-heated gas responsible for the observed time-variable 2–10 keV X-ray emission (Pittard & Corcoran 2002; Corcoran 2005; Hamaguchi et al. 2007; Okazaki et al. 2008; Corcoran et al. 2010; Parkin et al. 2009, 2011; Hamaguchi et al. 2014) that is a key signature

⋆ E-mail: clementel@strw.leidenuniv.nl

of a colliding wind binary (Luo, McCray & Mac Low 1990; Stevens, Blondin & Pollock 1992).

The WWC, orbital motion, and presence of η_B lead to numerous other forms of time-variable emission and absorption seen across a wide range of wavelengths (see e.g. Damineli et al. 2008a). Observational signatures that arise as a result of the WWC and η_B's ionizing radiation are important for studying η Car as they provide crucial information about the physical properties of the stars and the system as a whole. Three-dimensional (3D) hydrodynamical simulations show that the fast wind of η_B has a significant impact on shaping the wind of η_A (Okazaki et al. 2008; Madura 2010; Parkin et al. 2011; Madura & Groh 2012; Madura et al. 2012, 2013; Russell 2013), affecting greatly the observed optical and ultraviolet (UV) spectra of the system, as well as the interpretation of various line profiles and interferometric observables (Groh et al. 2010a,b, 2012a,b). Recently, Clementel et al. (2014, hereafter C14) presented 3D radiative transfer (RT) simulations that illustrate the effects of η_B's ionizing radiation on the outer regions of η Car's extended ($r \approx 1500$ au) colliding winds. However, to date there has been no detailed 3D RT modelling to determine the effects of η_B's ionizing radiation on η_A's inner wind, the inner wind–wind interaction region (WWIR), or the numerous observed emission and absorption lines that arise in the inner ∼150 au of the system.

A very important series of spectral features that have fascinated and perplexed researchers of η Car for decades are those due to helium. It was the periodic variation of the He I λ10830 emission line that originally led to the discovery of binarity in η Car (Damineli 1996; Damineli, Conti & Lopes 1997), and it is the disappearance of the narrow emission-line component of He I λ6678 that is typically used to define the starting point of a 5.54 yr spectroscopic cycle (Damineli et al. 2008b). Present-day broad wind lines of He I, most notably λ7067, are thought to be excited by the UV radiation of η_B and arise somewhere in/near the WWIR between the stars (Nielsen et al. 2007; Damineli et al. 2008b). Since the He I lines are recombination lines, they are produced in regions of He^+ rather than regions of neutral He. The locations of the strongest broad He I emission features are spatially unresolved in *Hubble Space Telescope* data, and almost certainly originate less than ∼100–200 au from η_A (Humphreys, Davidson & Koppelman 2008). The broad He I emission lines are consistently blueshifted throughout most of the 5.54 yr orbit and exhibit an interesting double peak profile that varies in intensity and velocity, especially across periastron passage (Nielsen et al. 2007).

The broad He I P Cygni absorption components also vary in velocity and strength over η Car's entire 5.54 yr period. The He I absorption is strongest in the two-year interval centred on periastron, and relatively weak at other phases (Nielsen et al. 2007). The absorption is always blueshifted, and hence must be produced by material between the observer and the continuum source η_A, although there is still some debate over whether the absorption is directly related to material in the WWIR (Damineli et al. 2008b) or produced by the pre-shock wind of η_A (Nielsen et al. 2007).

Further complicating the story is the observed gradual increase in the amount of P Cygni absorption over the last ∼10 yr. Since 1998, and most especially after the 2009 event, the strength of the He I absorption has increased compared to similar phases of previous cycles, while the emission strength has remained essentially unchanged (Groh & Damineli 2004; Mehner et al. 2010, 2012). Mehner et al. (2012) attribute this and other recent observed changes to a gradual decrease of η_A's mass-loss rate by a factor of ∼2–3 between 1999 and 2010. It is hypothesized that this decrease in η_A mass-loss rate led to important changes in the ionization structure of η_A's wind and the WWIRs, as caused by the presence of η_B (see e.g. fig. 5 of Mehner et al. 2012). However, this idea has yet to be quantitatively tested or modelled, and the results of 3D smoothed particle hydrodynamic (SPH) simulations appear to argue against such a large, gradual change in η_A's mass-loss rate (see Madura et al. 2013, hereafter M13).

Finally, there is the mystery regarding the origin of η Car's He II λ4686 emission, which is only seen strongly around periastron (between phases ∼ 0.98 and 1.03; Steiner & Damineli 2004; Martin et al. 2006; Mehner et al. 2011; Teodoro et al. 2012). The locations and physical mechanisms that give rise to this emission in η Car are not completely agreed upon, although several possible scenarios have been proposed (Steiner & Damineli 2004; Martin et al. 2006; Mehner et al. 2011; Teodoro et al. 2012; M13). The key difficulty with determining which scenario, if any, is correct is the lack of any detailed quantitative modelling of the 3D ionization structure of the innermost stellar winds and WWIR.

The goal of this paper is to compute full 3D RT simulations of the effects of η_B's ionizing radiation on η Car's inner winds and WWIR, focusing on the ionization structure of helium at orbital phases around apastron (i.e. the spectroscopic high state; Gull et al. 2009). The ionization structure of helium at periastron (the spectroscopic low state) is investigated in a subsequent paper (Clementel et al. MNRAS, submitted). We apply the SIMPLEX algorithm for 3D RT on an unstructured Delaunay grid (Ritzerveld & Icke 2006; Ritzerveld 2007; Kruip et al. 2010; Paardekooper, Kruip & Icke 2010; Paardekooper et al. 2011) to recent 3D SPH simulations of η Car's binary colliding winds that include orbital motion, radiative cooling, and radiative forces (M13). Using SIMPLEX, we obtain detailed ionization fractions of helium at the resolution of the original SPH simulations. This should help us determine much more precisely where, and to what extent, the various emission and absorption components of the observed broad helium lines can form. This paper lays the foundation for future work aimed at generating synthetic spectra for comparison to observational data. We note that we focus solely on interpreting the *broad* emission and absorption features of helium that arise in the stellar winds and WWIRs, and not the much narrower ($\lesssim 50$ km s^{-1}) features that form in the Weigelt blobs and other dense, slow-moving near-equatorial circumstellar ejecta (Weigelt & Ebersberger 1986; Damineli et al. 2008b).

We describe our numerical approach, including the SPH simulations, the SIMPLEX code, and the RT simulations in Section 2. Section 3 describes the results. A discussion of the results and their implications is in Section 4. Section 5 summarizes our conclusions and outlines the direction of future work.

2 METHODS

2.1 The 3D SPH simulations

The hydrodynamical simulations used in this work correspond to the three small-domain ($r = 10a = 155$ au) 3D SPH simulations of M13. This computational domain size was chosen in order to investigate, at sufficiently high resolution, the structure of η Car's inner WWIRs and their effects on η_B's ionizing radiation since the 'current' interaction between the two winds occurs at spatial scales comparable to the semi-major axis length $a \approx 15.4$ au ≈ 0.0067 arcsec at $D = 2.3$ kpc. In the following, we briefly describe only the essential aspects of the SPH code and setup. We refer the reader to M13 and references therein for further details.

Table 1. Stellar, wind, and orbital parameters of the 3D SPH simulations

Parameter	$\eta_{\rm A}$	$\eta_{\rm B}$
$M_\star$ ($M_\odot$)	90	30
$R_\star$ ($R_\odot$)	60	30
$\dot{M}$ (10^{-4} $M_\odot\,yr^{-1}$)	8.5, 4.8, 2.4	0.14
v_∞ ($km\,s^{-1}$)	420	3000
η	0.12, 0.21, 0.42	
$P_{\rm orb}$ (d)	2024	
e	0.9	
a (au)	15.45	

Notes: $M_\star$ and $R_\star$ are the stellar mass and radius. $\dot{M}$ and v_∞ are the stellar-wind mass-loss rate and terminal speed, respectively. $\eta \equiv (\dot{M}v_\infty)_{\eta_{\rm B}}/(\dot{M}v_\infty)_{\eta_{\rm A}}$ is the secondary/primary wind momentum ratio, $P_{\rm orb}$ is the orbital period, e is the eccentricity, and a is the length of the orbital semimajor axis.

Radiative cooling is implemented using the Exact Integration Scheme of Townsend (2009), with the radiative cooling function $\Lambda(T)$ calculated using CLOUDY 90.01 (Ferland et al. 1998) for an optically thin plasma with solar abundances. The pre-shock stellar winds and rapidly-cooling dense gas in the WWIRs are assumed to be maintained at a floor temperature = 10^4 K due to photoionization heating by the stars (Parkin et al. 2011). Radiative forces are incorporated via the 'antigravity' formalism described in M13 and Russell (2013). We parametrize the stellar winds using the standard 'beta-velocity law' $v(r) = v_\infty(1-R_\star/r)^\beta$, where v_∞ is the wind terminal velocity, $R_\star$ the stellar radius, and β (= 1) a free parameter describing the steepness of the velocity law. Effects due to radiative braking (Gayley, Owocki & Cranmer 1997; Parkin et al. 2011), photospheric reflection (Owocki 2007), and self-regulated shocks (Parkin & Sim 2013), are not included since such effects are not expected to play a prominent role in η Car (Parkin et al. 2009, 2011; Russell 2013; M13). We include the more important velocity-altering effects of 'radiative inhibition' (Stevens & Pollock 1994; Parkin et al. 2009, 2011). However, possible changes to the mass-loss rates due to radiative inhibition are not included. These are not expected to be significant in η Car and should not greatly affect our results or conclusions (M13).

We use a standard *xyz* Cartesian coordinate system and set the orbit in the *xy* plane, with the origin at the system centre of mass and the major axis along the *x*-axis. The stars orbit counter-clockwise when viewed from along the +*z*-axis. By convention, t = 0 ($\phi = t/2024 = 0$) is defined as periastron. Simulations are started at apastron and run for multiple consecutive orbits.

The outer spherical simulation boundary is set at $r = 10a$ from the origin. Particles crossing this boundary are removed from the simulations. The adopted simulation parameters (Table 1) are consistent with those derived from the available observations, although there is some debate on the present-day value of $\dot{M}_{\eta_{\rm A}}$ (see M13 for details). In an attempt to better constrain $\dot{M}_{\eta_{\rm A}}$, M13 performed a series of 3D SPH simulations assuming three different $\dot{M}_{\eta_{\rm A}}$. We use the same naming convention as M13 when referring to the SPH and SIMPLEX simulations in this paper, namely, Case A ($\dot{M}_{\eta_{\rm A}} = 8.5\times10^{-4}$ $M_\odot\,yr^{-1}$), Case B ($\dot{M}_{\eta_{\rm A}} = 4.8\times10^{-4}$ $M_\odot\,yr^{-1}$), and Case C ($\dot{M}_{\eta_{\rm A}} = 2.4\times10^{-4}$ $M_\odot\,yr^{-1}$).

2.2 The SIMPLEX algorithm for RT on an unstructured mesh

For the RT calculations, we post-process the 3D SPH simulation output using the SIMPLEX algorithm (Ritzerveld & Icke 2006; Ritzerveld 2007; Kruip et al. 2010; Paardekooper, Kruip & Icke 2010; Kruip 2011). We employ a methodology nearly identical to that in C14, but use an updated version of SIMPLEX, which contains several important improvements over the version used in C14. We discuss the relevant differences in the following sections, and briefly describe the key aspects of the code and their relevance to this work. We refer the reader to C14 and references therein for further details on SIMPLEX and its applications.

2.2.1 *Grid construction and density distribution*

As in C14, we use the SPH particles themselves as the generating nuclei for the Voronoi–Delaunay mesh. We assign to the nucleus of each Voronoi cell the corresponding SPH density, computed using the standard SPH cubic spline kernel (Monaghan 1992). This helps ensure that the number density used in the SIMPLEX calculations closely matches that of the original SPH simulations. Note that this approach differs from that used by C14, wherein the SIMPLEX density is obtained by dividing the SPH particle mass by the corresponding Voronoi cell volume. Using the SPH kernel produces smoother densities than the Voronoi cell-volume approach, since the SPH kernel samples a larger number of particles over a larger volume, resulting in densities that are less affected by local differences in the SPH particle distribution (see Fig. 1). Comparison with a direct visualization of the SPH density output (using SPLASH, Price 2007, left-hand panel of Fig. 1) shows that the SPH kernel approach indeed matches better the density distribution of the original SPH simulations. Fig. 2 shows an example of the SIMPLEX mesh and number density at apastron for a representative 3D SPH simulation of η Car.

2.2.2 *Ionization state and chemistry of the gas*

As in C14, we perform the RT calculations in post-processing. We consider the ionization of hydrogen and helium atoms by both photo- and collisional ionization. The ionization rate equations are solved on a time-step smaller than the RT time-step to ensure photon conservation (Pawlik & Schaye 2008; Paardekooper, Kruip & Icke 2010). This can lead to very small time-steps in cells where the photoionization time-scale is very small. To speed up the computation in these cells, we instead use the time-averaged optical depth to compute the photoionization rate and iterate for convergence (Mellema et al. 2006; Friedrich et al. 2012).

2.2.3 *Treatment of the ionizing spectrum and transport method*

In numerical simulations involving radiation it is necessary to approximate the continuous spectrum of radiation with a finite number of discrete frequency bins due to memory requirements. In C14, the extreme limit of a single frequency bin, commonly referred to as the 'grey approximation', was used. Although in the grey approximation all spectral information is lost, it is still possible to enforce the conservation of a quantity of importance such as the number of ionizations per unit time or the energy deposition into the medium per unit time. However, since in this work we are interested in the detailed ionization structure of He, and we want to capture the behaviour of the product of the spectrum and cross-sections in sufficient detail, we now employ three frequency bins.

The width of each frequency bin is set by the ionization energy of each species. The first bin ranges from the ionization frequency

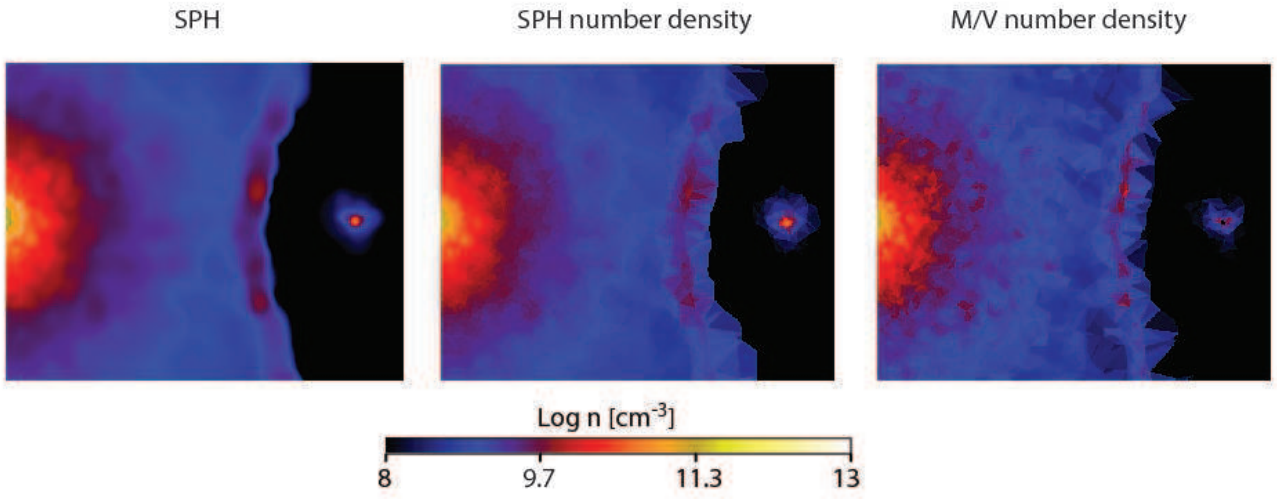

Figure 1. Zoom of the central region for a slice in the *xy* orbital plane through the 3D simulation volume for the Case A simulation at apastron. Colour shows number density on a logarithmic scale (cgs units) using three different visualization approaches (see Section 2.2.1). Left-hand panel: direct visualization using SPLASH. Middle panel: SPH kernel approach. Right-hand panel: SPH particle mass divided by Voronoi cell volume approach.

of H^{0+} ($\nu_{H^{0+}} = 3.28\times10^{15}$ Hz) to that of He^{0+} ($\nu_{He^{0+}} = 5.93\times10^{15}$ Hz), the second from $\nu_{He^{0+}}$ to $\nu_{He^{+}}$ (1.31×10^{16} Hz), and the third from $\nu_{He^{+}}$ to a maximum frequency equal to 10 times $\nu_{H^{0+}}$. We use an effective cross-section representation to determine the correct number of absorptions within each frequency bin. In this case, the limits of integration in equations 7 and 8 of C14 are over the frequency range of the bin of interest.

In C14, photons were transported across the SIMPLEX grid using ballistic transport. With this method, the incoming direction of the photons is used to define the outgoing direction, and the outgoing photons are distributed in 3D over the three most forward edges of the Delaunay triangulation. One drawback of this approach is that, due to the random nature of the outgoing directions in the Delaunay grid, the radiation may lose track of the original incoming direction after many steps. If the cells are optically thin, this can result in a radiation field that is too diffusive, leading to overestimates of the ionization fractions. To solve this problem, the original direction of the photons is preserved by confining them to solid angles corresponding to global directions in space. This is known as direction-conserving transport (DCT; Kruip et al. 2010; Paardekooper 2010).

In DCT, if a photon is emitted in a certain direction associated with a solid angle, it will remember this direction and, unless it interacts with atoms on the grid, it will stay in the same solid angle as it travels through the grid. This effectively decouples the directionality of the radiation field from the directions present in the grid. In this work, we use 84 directions with DCT, implying a solid angle of $\pi/21$ sr for each unit vector.

2.2.4 *The ionizing source η_B*

Based on Mehner et al. (2010), Verner, Bruhweiler & Gull (2005) and Madura et al. (2012), we consider η_B to be an O5 giant with $T_{eff} \approx 40{,}000$ K. We assume a total ionizing flux for H and He of 3.58×10^{49} photons s^{-1} (Martins, Schaerer & Hillier 2005).

As described in Section 2.2.3, we use three bins to sample the spectrum, which we approximate with a blackbody. We are therefore interested in the number of ionizing photons in each bin, photons$_i$, which depends on the blackbody temperature:

$$\text{photons}_i = \int_0^{\lambda_i} B_\lambda(T)\mathrm{d}\lambda, \quad (1)$$

where the λ_i are the limiting wavelengths for the ionization of H^{0+} ($\lambda = 912$ Å), He^{0+} ($\lambda = 504$ Å) and He^{+} ($\lambda = 228$ Å), and B_λ is the Planck spectrum

$$B_\lambda(T) \propto (\lambda^5 \exp[hc/(\lambda k_B T)])^{-1}. \quad (2)$$

In Martins, Schaerer & Hillier (2005), the fluxes able to ionize H and He are defined as

$$q_i = \int_0^{\lambda_i} \frac{\pi\lambda F_\lambda}{hc}\mathrm{d}\lambda, \quad (3)$$

where F_λ is the flux expressed in erg/s/cm^2/Å. We set the blackbody temperature to the value that produces the correct ratio photons$_{H^{0+}}$/photons$_{He^{0+}}$ (in this case $T_{bb} = 49{,}000$ K), in accordance to the $q_{H^{0+}}/q_{He^{0+}}$ ratio in Martins, Schaerer & Hillier (2005). $q_{He^{+}}$ is effectively zero for η_B.

2.2.5 *Visualization of the unstructured mesh results*

When visualizing the SIMPLEX simulation output, we would ideally like to render physical quantities that are centred on the original Voronoi cells that compose our 3D unstructured grid. Unfortunately, the Voronoi cells consist of a series of irregular *n*-sided polygons, which makes their visualization quite complex. Instead, it is much more straightforward to visualize the corresponding Delaunay triangulation. In 3D, the Delaunay cells are tetrahedra, which can be visualized using standard visualization tools such as VISIT[1]. Since the Delaunay cells are tetrahedra, the quantity we visualize

[1] https://wci.llnl.gov/simulation/computer-codes/visit

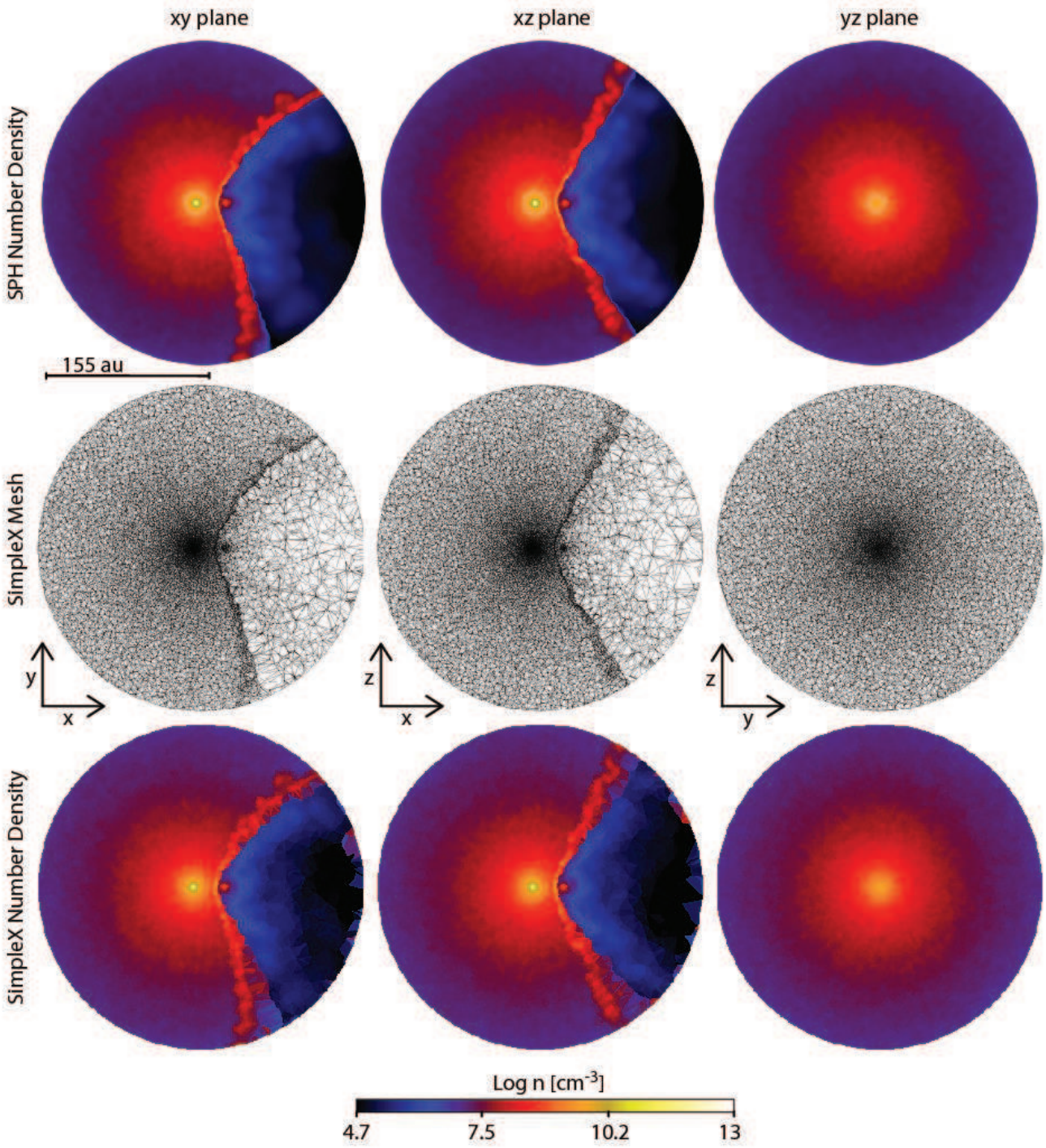

Figure 2. Slices in the *xy* (left-hand column), *xz* (middle column) and *yz* (right-hand column) planes through the 3D simulation volume for the Case A simulation at apastron. Rows show, from top to bottom, the original SPH number density distribution (log scale, cgs units), the SIMPLEX mesh, and the resulting SIMPLEX number density (same log scale, cgs units). The resolution of the SIMPLEX mesh, as well the number density, follow well the resolution of the original SPH data. The length-scale is shown under the top-left panel. In the first column (i.e. the orbital plane) η_A is to the left and η_B is to the right.

is the average of the four vertices that define the tetrahedron cell (i.e. the average of the four Voronoi nuclei). This approach works well for visualizing most physical quantities (e.g. temperature, density, velocity). However, if neighbouring Voronoi nuclei have values which are significantly different (i.e. by several orders of magnitude), this 'volume-average' approach may lead to tetrahedral-cell values that are difficult to interpret.

Unfortunately, the fractions of He^{0+}, He^{+}, and He^{2+} can span 10 or more orders of magnitude across the WWIR in η Car. The volume-averaged fractions in the larger grid cells that define the post-shock secondary wind can therefore be difficult to understand,

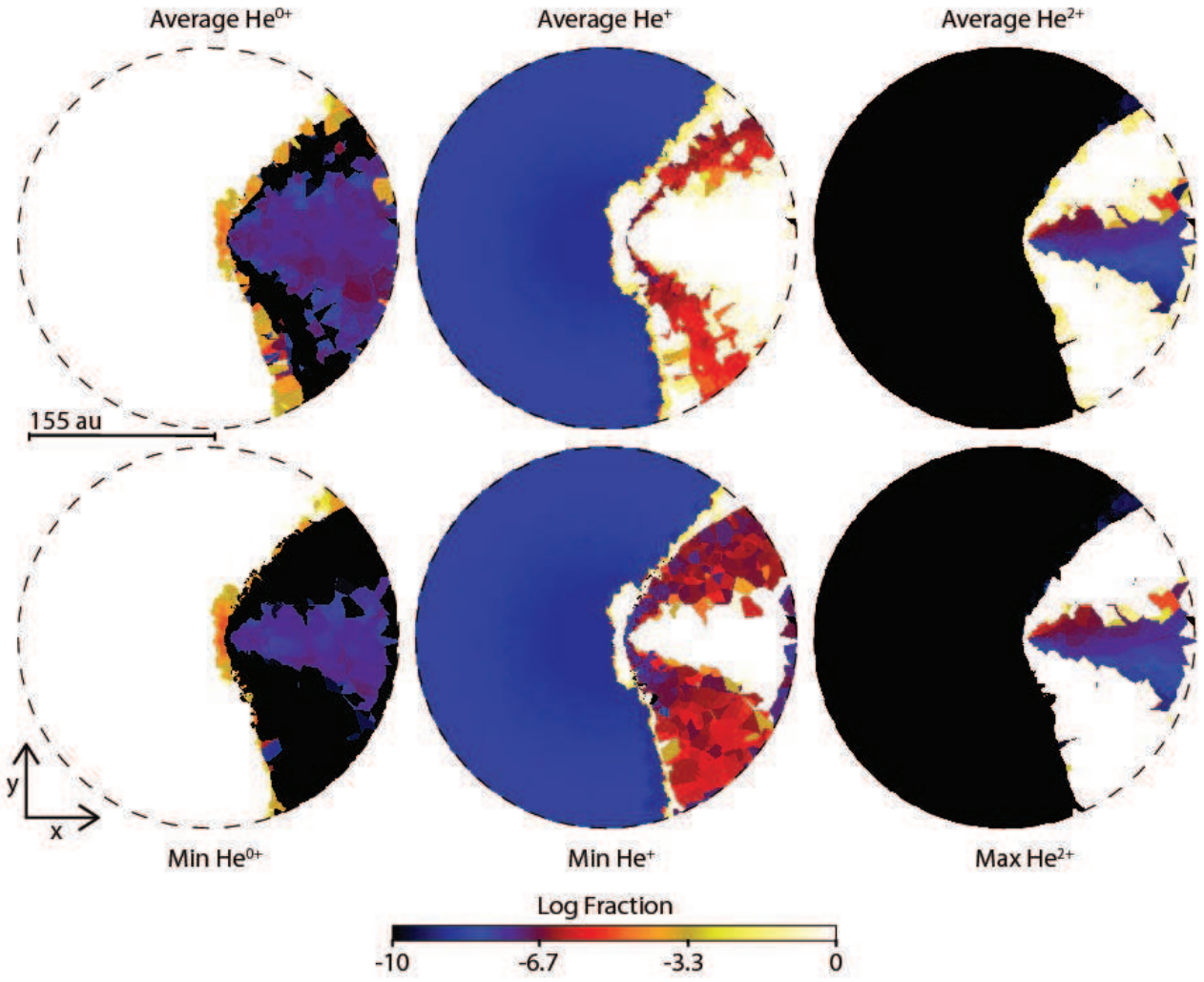

Figure 3. Slice in the *xy* orbital plane through the 3D simulation volume for the Case A simulation at apastron. Columns show, from left to right, the computed fractions of He^{0+}, He^{+} and He^{2+} (log scale). Images in the top row were computed using the volume average approach (see Section 2.2.5). Images in the bottom row show, from left to right, the minimum He^{0+}, minimum He^{+} and maximum He^{2+} values and extents. In this and future plots, the dashed circle marks the edge of the spherical computational domain.

especially when a logarithmic colour scale is used (see Fig. 3). As an example, consider the fraction of He^{+} near the contact discontinuity (CD) in the WWIR. If three of the vertices of a tetrahedron cell are highly ionized and have extremely low fractions of He^{+} ($\lesssim 10^{-10}$), while the fourth vertex has a large fraction of He^{+} (≈ 1), the final He^{+} fraction visualized over the *entire* cell will be ~0.25. This simply tells us that ~ 25% of the cell's volume is He^{+}. The problem is that the visualization of the He^{+} fraction alone tells us nothing about *which* ~25% of the cell volume is He^{+}, nor does it tell us directly what percentage of the remaining ~75% of the cell volume is He^{0+} or He^{2+}. Therefore, while correct, the visualized plots of various ionization fractions can be deceiving, since for certain species they give the appearance of physically incorrect locations for the ionization fronts. In our He^{+} example, there appears to be a thick region of He^{+} near the CD in the hot, post-shock secondary wind (top-middle panel of Fig. 3), even though the gas in this region is extremely hot ($\gtrsim 10^{6}$ K, see Fig. 5), and should consist entirely of He^{2+}.

Therefore, instead of the average, we show the minimum vertex value for the fraction of He^{0+} and the maximum vertex value for the fraction of He^{2+}. For He^{+}, we show the maximum value whenever the tetrahedron consists of vertices that are only from the primary wind, and the minimum otherwise (if we were to simply show the minimum of the He^{+} fraction everywhere, we would underestimate the penetration of $\eta_{\rm B}$'s He-ionizing radiation into $\eta_{\rm A}$'s pre-shock wind). This choice for visualizing our simulations shows an *upper* limit to the ionization state of He, in the sense that it shows the maximum extent of the ionization front (bottom row of Fig. 3). By using this approach, the ionization structure of He much better follows the temperature structure of the gas (Fig. 5) in places where collisional ionization dominates. Therefore, the physics in our simulations is more truthfully represented. We emphasize that the visualizations are merely to help guide the reader, and neither the physics nor the conclusions of our work depend on them.

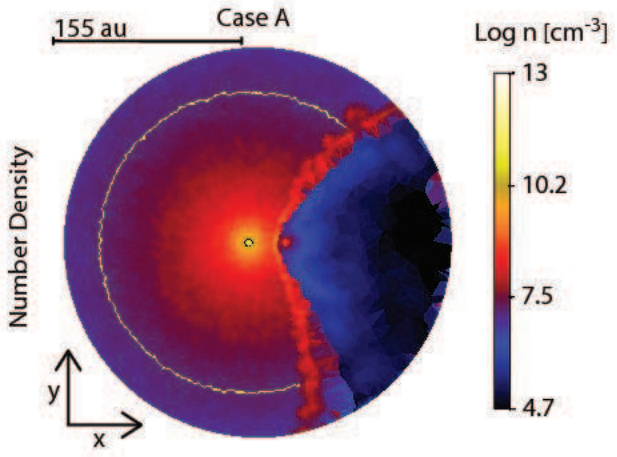

Figure 4. Slice in the *xy* orbital plane through the 3D simulation volume for the Case A simulation at apastron. The black (r = 3 au) and yellow (r = 120 au) lines indicate the He^+ and H^+ ionization radii in the pre-shock η_A wind for simulation Case A, based on the CMFGEN models of Hillier et al. (2001, 2006) and Groh et al. (2012a). Radii for Case B are only marginally larger than shown. For Case C, the He^+ radius is comparable to the yellow line (see Fig. 7), while H is H^+ throughout the entire simulation domain.

2.3 Application to η Car

We focus on the ionization of He at an orbital phase of apastron assuming the same abundance by number of He relative to H as Hillier et al. (2001), $n_{He}/n_H = 0.2$. We employ a single photoionizing source located at the position of η_B. Details on the nature and implementation of the η_B spectrum are described in Section 2.2.4.

Collisional ionization equilibrium of the SPH simulation snapshot is used as an initial condition for the SIMPLEX simulations. The SPH output is post-processed with SIMPLEX until the ionization state reaches an equilibrium value (this typically happens within ~1–2 months of simulation time). We use a simulation time-step of ~5 min, which is sufficiently small for accurate RT calculations of the ionization volumes and fractions.

For simplicity, we neglect the influence of the WWIR X-rays on the He ionization structure at times around apastron since they are highly inefficient at ionizing He (C14).

2.3.1 Influence of η_A

As in C14, we neglect the η_A ionizing source for simplicity. We also do not consider the ionization structure of hydrogen (although it is included in our calculations). In this work, we focus on the influence of η_B's He-ionizing radiation on the WWIRs and η_A's pre-shock wind. Hillier et al. (2001, 2006) and Groh et al. (2012a) fitted the optical and UV spectra of η_A and computed the ionization structure of H and He within the optically-thick wind of η_A for different $\dot{M}_{\eta_A}$. They found that the H^+ region around η_A extends radially ~120–125 au for simulation Cases A ($\dot{M}_{\eta_A}$ = 8.5×10^{-4} $M_\odot\,yr^{-1}$; see e.g. the yellow line in Fig. 4) and B ($\dot{M}_{\eta_A}$ = 4.8×10^{-4} $M_\odot\,yr^{-1}$). For Case C ($\dot{M}_{\eta_A} = 2.4\times10^{-4}$ $M_\odot\,yr^{-1}$), hydrogen is fully ionized throughout the entire η_A wind ($r \gtrsim 5500$ au).

Due to the smaller domain size of the simulations used in this paper (r = 155 au), and because η_B will fully ionize H^{0+} throughout its wind, little information is gained by examining the ionization structure of hydrogen in our simulations. In principle, we might gain information about the ionization state of H in the cold, post-shock η_A gas, but this depends strongly on the population of the $n = 2$ state of H^{0+} in this region and the η_A ionizing source. Lower energy (10.2 eV) photons could populate the $n = 2$ state of any H^{0+} in the post-shock η_A gas, which could then be ionized to H^+ by 3.4 eV photons. Thus, it is possible that H is ionized everywhere in the inner ~120–150 au region around η_A, including the WWIRs.

In contrast, He is mainly neutral in the wind of η_A. As shown in Fig. 4 (black line), the extent of the He^+ region in η_A's wind, for Cases A (r ~ 3 au) and B (r ~ 7.5 au), is much smaller (Hillier et al. 2001, 2006; Groh et al. 2012a). The energy level structure of He is such that high-energy photons (~19.8 eV) are needed to populate even the lowest excited states (Nielsen et al. 2007). η_B is the only known source of such photons in η Car. He I lines are thought to represent the highly excited regions of η_A's wind and/or the WWIR (Nielsen et al. 2007). It may be the case that He^{0+}-ionizing photons from η_B are able to penetrate the WWIRs and reach the He^+ region deep within η_A's wind. The inner η_A He^+ region would be effectively transparent to such photons, which may allow them to pass through to the He^{0+} zone on the back side of η_A (the side facing away from η_B). Thus, determining the correct overall He ionization structure requires some method of mimicking the internal ionization structure of He in η_A's pre-shock wind due solely to η_A.

The simplest method, which we employ for this work, is to set as an initial condition to the SIMPLEX simulations the ionization structure of He^+ in η_A's inner wind. To do this, we set the temperature in the innermost η_A wind to 50,000 K, which is hot enough to singly-ionize He^{0+} to He^+, but not He^{2+}. The outer radius of this inner He^+ region for each simulation case is set to the appropriate value based on the 1D CMFGEN models of η Car by Hillier et al. (2001, 2006), namely, 3 au, 7.5 au, and 120 au for Cases A, B, and C, respectively (see Fig. 7). We do not include the inner He^{2+} zone in η_A's wind since in most cases it is of negligible size (r < 1 au), and because η_B produces essentially zero He^+-ionizing photons.

3 RESULTS

Figs. 5 and 6 display the number density and temperature in the orbital and *xz* planes for simulation Cases A–C. Due to the smaller spatial size of these simulations, the density and temperature structures are less complex than those described in C14. As shown by Okazaki et al. (2008), Parkin et al. (2011), Madura & Groh (2012), Madura et al. (2012, 2013), the lower density faster η_B wind carves a large cavity out of the slower, denser wind of η_A for the majority of the orbital period. Around apastron, this cavity and the WWIR have an nearly axisymmetric conical shape, with the opening angle increasing as the value of $\dot{M}_{\eta_A}$ decreases. The apex of the WWIR also moves closer to η_A as $\dot{M}_{\eta_A}$ is lowered, due to the change in wind momentum balance. The WWIR consists, on the secondary side of the CD (right-hand side of the panels), of a distended shock containing hot ($T \gtrsim 10^6$–10^8 K) low-density η_B wind material. On the primary side of the CD, the post-shock η_A gas (green contours) is much thinner and colder ($T \approx 10^4$ K).

The bottom row of Figs. 5 and 6 show that, in the orbital plane, the overall fraction of η_B's wind that is shock heated increases, relative to the total area of secondary wind, with $\dot{M}_{\eta_A}$. Additionally, the amount of the hottest gas (in red) located in the arms of the WWIR increases as $\dot{M}_{\eta_A}$ decreases. This happens because, for a given pre-shock wind speed, more oblique shocks (i.e. Case A versus Cases B and C) produce lower post-shock temperatures (Pittard 2009; M13). For all three $\dot{M}_{\eta_A}$, the hottest gas is located at the apex of the WWIR. However, there is an asymmetry in the temperature

of the post-shock η_B gas in the arms of the WWIR, with the gas in the leading arm hotter than the gas in the trailing arm. This is a result of the different pre-shock wind speeds in the two arms, caused by the orbital motion. The wind in the direction of orbital motion has an additional component added to its velocity, due to the velocity of the star about the system centre of mass. In the opposite direction of orbital motion, this component is subtracted, so that the wind is slightly slower in that direction, and therefore the shock slightly cooler. The post-shock η_A wind region appears to become slightly thinner and less dense the lower the value of $\dot{M}_{\eta_A}$, and the WWIR seems to become more unstable. However, standard SPH schemes are known for under resolving certain hydrodynamic instabilities (Agertz et al. 2007; Price 2008), so these results should be interpreted with caution. For further details on the density and temperature structures of the winds and the effects of different $\dot{M}_{\eta_A}$, see M13.

To help provide a scale comparison with the larger domain simulations of C14, we point out that the remnant of the expanding shell of η_A wind created during the previous periastron passage (as described in M13) is visible at the outer edge of the simulation domain on the apastron side of the system (see the shock-heated gas in the bottom row of Figs. 5 and 6). Furthermore, to assist the reader in interpreting the He ionization plots, we have outlined the location of the cold, dense, post-shock η_A wind in Figs. 5–8 using a green contour. Finally, we note that, as illustrated in the rightmost column of Fig. 2, on this simulation scale, slices in the *yz* plane through the system centre of mass only sample the pre-shock wind of η_A. They thus provide little new relevant information on the ionization structure of He at apastron. Hence, we focus our discussion on the results in the orbital (*xy*, Fig. 7) and *xz* (Fig. 8) planes.

3.1 Overall He Ionization Structure and Influence of $\dot{M}_{\eta_A}$

3.1.1 The orbital plane

Fig. 7 illustrates the fractions of He^{0+}, He^{+} and He^{2+} (rows, top to bottom) in the orbital plane for the three $\dot{M}_{\eta_A}$ simulations (Cases A–C, from left to right). In all three cases, on the secondary side of the WWIR, the ionization state of the high temperature shock-heated gas is dominated by collisional ionization. At such high temperatures ($T \gtrsim 10^6$ K) helium is fully-ionized to He^{2+} (white area in the bottom row). The unperturbed expanding secondary wind located between the two arms of the WWIR is, instead, principally composed of He^{+} due to photoionization by η_B. This is an expected difference, compared to the results in C14, connected with the better approximation of the η_B spectrum using three frequency bins. As discussed in Section 2.3.1, η_B should not produce many He^{+}-ionizing photons. Therefore, the low fraction of He^{2+} in its unshocked wind is expected. Note also that there is no He^{2+} in the pre- and post-shock primary wind, as expected. He^{2+} thus appears to be an excellent tracer of the hot, post-shock η_B wind region. One important consequence of the larger opening angle of the WWIR for lower $\dot{M}_{\eta_A}$ is an increase in the volume of the He^{+} region in η_B's wind on the apastron side of the system, and an increase in the angle between the two arms of He^{2+}.

While the situation on the η_B-side of the system does not depend strongly on $\dot{M}_{\eta_A}$, the He structures on the periastron (η_A) side of the system are quite different for the three $\dot{M}_{\eta_A}$. Our simulations show that the He^{0+}-ionizing photons are able to penetrate into the unperturbed primary wind to varying degrees for all $\dot{M}_{\eta_A}$, but the detailed results depend drastically on $\dot{M}_{\eta_A}$. In Case A, the He^{+} structure is much smaller and closer to the WWIR apex than in Cases B–C. Aside from this central area around the apex of the WWIR, the He^{+} front appears to extend only about half way into the post-shock primary wind. *Most importantly, there is no layer of He^{+} in the pre-shock η_A wind that borders the entire WWIR*. This is in contrast to the simple models proposed by e.g. Martin et al. (2006), Humphreys, Davidson & Koppelman (2008), and Mehner et al. (2012). The cold, dense, post-shock η_A wind, in our simulation, absorbs most of the He^{0+}-ionizing photons from η_B.

The middle row of Fig. 7 shows that a decrease in $\dot{M}_{\eta_A}$ leads to a deeper penetration of the He^{0+}-ionizing photons into the primary wind and, consequently, a much larger volume of He^{+} on the primary side of the system. η_B is able to effectively ionize a significant volume of the primary wind in Case B (the edge of the ionization front is just visible at the bottom edge of the panel in the pre-shock primary wind), while in Case C, η_B is able to ionize He in nearly the entire pre- and post-shock primary wind (on this simulation domain scale). Note also the 'bent wing' geometry of the He^{+} ionization front that penetrates into η_A's pre-shock wind in Case B, which is caused by the radial dependence of the density in η_A's wind.

The introduction of the inner He^{+} region (due to η_A photoionization, see Section 2.3.1) has no noticeable effect on the He ionization structure for Cases A and B (middle row of Fig. 7). In both cases, He^{0+}-ionizing photons from η_B are unable to reach the deepest parts of the pre-shock primary wind. On the other hand, the much larger ionized sphere in Case C ($r = 120$ au) further increases the volume of He^{+} in η_A's wind. The black line, in the right-hand panel of the middle row of Fig. 7, marks the area that is He^{0+} when the ionization due to η_A is excluded from our calculations. As one would expect, when the influence of η_A is neglected, as $\dot{M}_{\eta_A}$ decreases, a larger volume is ionized. Only a narrow column focused directly behind and away from η_A remains neutral.

In Cases A and B, there is also a noticeable asymmetry in ionization between the leading and trailing arms of the WWIR. The leading arm shows a higher (in value) and wider (in spatial extent) presence of He^{+}, both in the post-shock primary wind and the unperturbed primary wind. A possible explanation for this difference might be found in the slight differences in temperature and density between the two arms. Since the leading arm of the WWIR has higher gas temperatures, He^{0+}-ionizing photons may be able to more easily penetrate the post-shock η_B gas in the leading arm, causing more ionization of the pre- and post-shock η_A wind.

3.1.2 The xz plane

Fig. 8 shows the fractions of He^{0+}, He^{+}, and He^{2+} in the *xz* plane for Cases A–C. The ionization structure in this plane exhibits the same trends, as a function of $\dot{M}_{\eta_A}$, as the orbital plane. This is expected due to the nearly axisymmetric nature of the WWIR around apastron. However, there is one striking difference, namely, the structure of He^{+} in the Case B simulation. In this case, the He^{+} structures on the primary side of the CD are much smaller in the *xz* plane than those in the orbital plane. We speculate that this may be due to the less turbulent nature of the WWIR in the plane perpendicular to the orbital motion. Instabilities in the WWIR may be more prevalent in the orbital plane, causing gaps to arise in the post-shock η_A wind that allow He^{0+}-ionizing photons from η_B to more easily penetrate into the pre-shock η_A wind. However, detailed studies of the 3D structure of complex WWIRs (like those in η Car) in regions above and below the orbital plane, and how various instabilities affect this structure, currently do not exist in

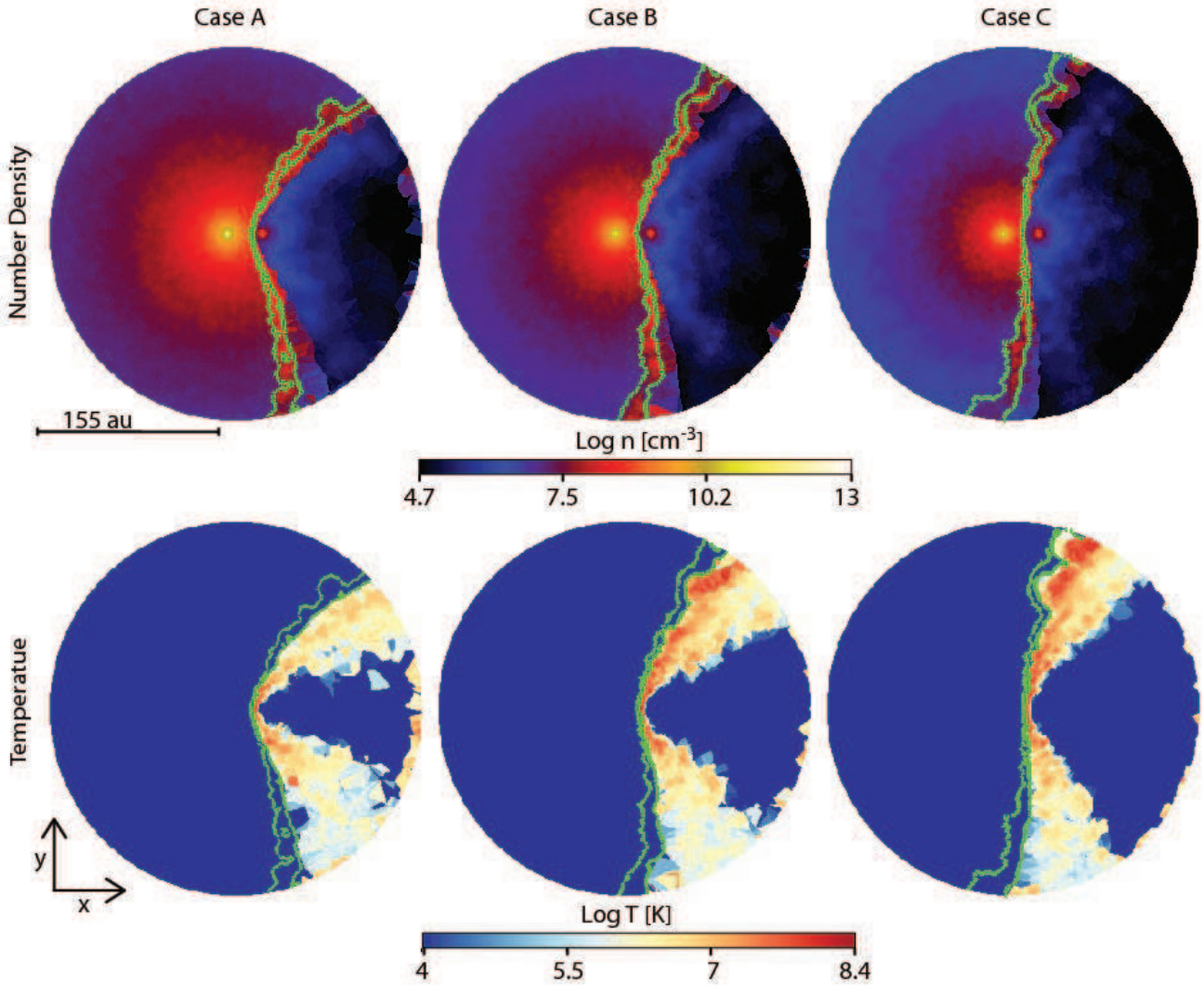

Figure 5. Slices in the orbital plane through the 3D SIMPLEX simulation volume for the three different assumed $\dot{M}_{\eta_A}$ (columns, left to right; Case A = 8.5×10^{-4} $M_\odot\,yr^{-1}$, Case B = 4.8×10^{-4} $M_\odot\,yr^{-1}$, and Case C = 2.4×10^{-4} $M_\odot\,yr^{-1}$). Top row shows the SIMPLEX number density (log scale, cgs units), while the bottom row shows the temperature (log scale, K). In this and future plots, the green contour highlights the location of the cold, dense, post-shock primary wind region.

the literature. Future detailed simulations of such 3D WWIRs are necessary to determine if our interpretation is correct.

4 DISCUSSION

Our SIMPLEX results show that, assuming for η_B a typical ionizing flux appropriate for an O-type star with $T_{eff} \approx 40,000$ K, η_B singly-ionizes He throughout its unshocked wind, as expected. Moreover, extremely high temperatures ($\gtrsim10^6$ K) cause He to be doubly-ionized in the post-shock η_B gas. Our results also help rule out very low values of $\dot{M}_{\eta_A}$ approaching 2.4×10^{-4} $M_\odot\,yr^{-1}$. Our Case C simulations show that for such low $\dot{M}_{\eta_A}$, η_B is able to singly-ionize He throughout practically our entire computational domain, including the dense pre- and post-shock primary wind regions. The ionized volume is even bigger if one includes the He ionization structure of η_A's inner wind, wherein η_A already singly-ionizes He out to a radius of ~120 au in its wind (Hillier et al. 2001, 2006). This makes it easier for ionizing photons from η_B to penetrate η_A's wind and enlarge the He ionization zone. In such a scenario, one would expect a significant amount of He II λ4686 emission from the dense, ionized primary wind and WWIR, even around apastron, which is not observed (Hillier et al. 2006; Teodoro et al. 2012). The strength of the emission in the broad He I lines is also expected to be much stronger than observed if $\dot{M}_{\eta_A}$ were so low (Hillier et al. 2006).

A similar situation is envisioned in Case B, namely, stronger He I and He II emission lines compared to Case A. This is true even though the inner He^+ ionization radius produced by η_A in its wind is much smaller than in Case C. However, He^{0+}-ionizing photons are still able to penetrate the dense WWIR and ionize a significant volume of η_A's pre-shock wind. Determining the strength of such He emission lines in Case B is beyond the scope of this paper, so we unfortunately cannot rule out at this time that such emission would be in direct disagreement with observations. Still, we would naively expect, based on our results, significant detectable He II emission at times around apastron, which is currently not observed. Thus,

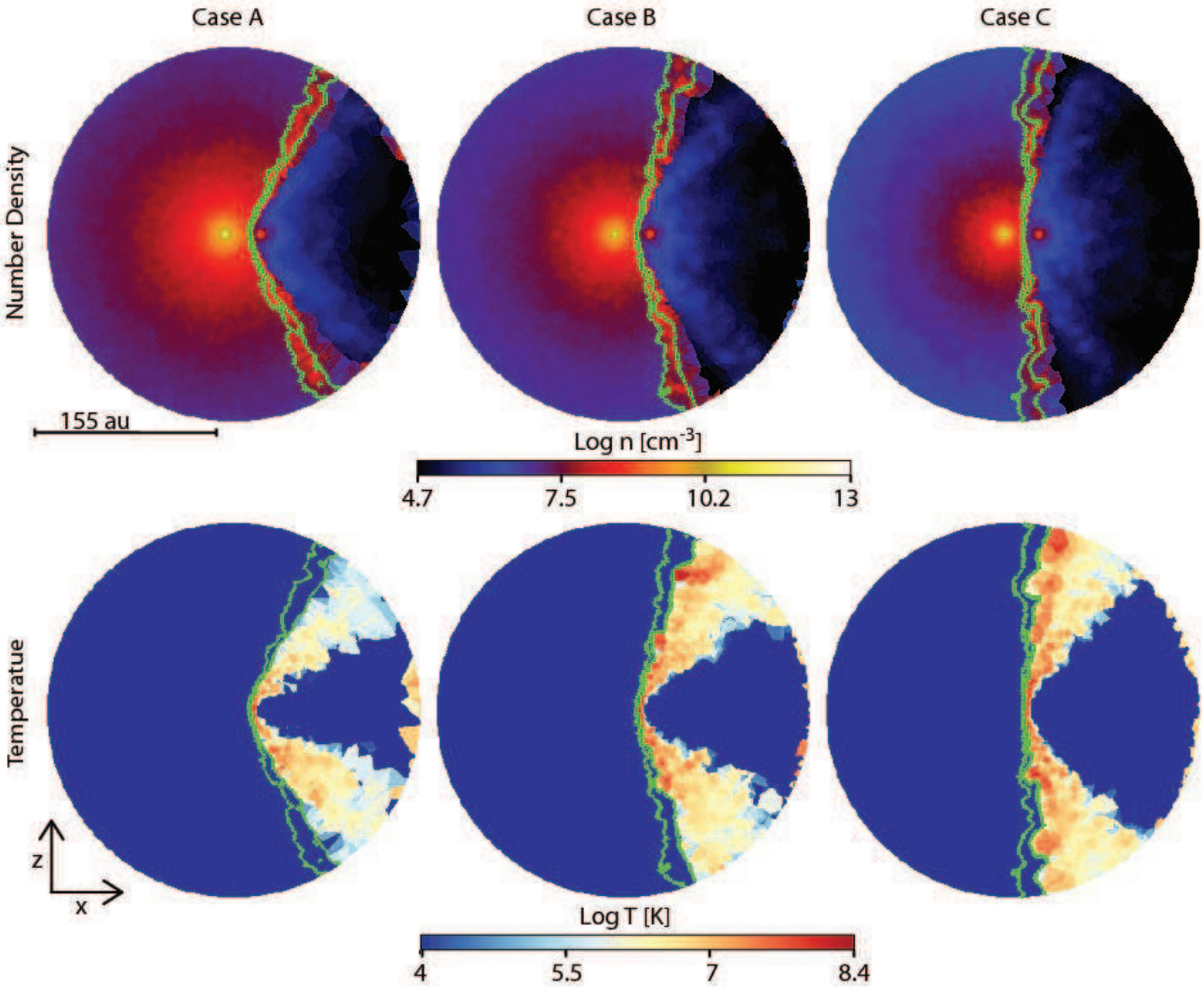

Figure 6. Same as Fig. 5, but for slices centred in the *xz* plane.

Case B (4.8×10^{-4} $M_\odot\,yr^{-1}$) may represent a lower limit on the current value of $\dot{M}_{\eta_A}$.

The location of the He^+ region in our simulations provides further support for binary orientations in which apastron is on our side of the system (e.g. Damineli et al. 2008a; Okazaki et al. 2008; Parkin et al. 2009, 2011; Madura et al. 2012). The observed He I emissions in η Car are primarily blueshifted along most of the 5.5 yr cycle, and the P Cygni absorptions (which must be formed on our side of η_A, the continuum source) are weak for most of the cycle (Hillier et al. 2001, 2006; Nielsen et al. 2007; Damineli et al. 2008a). Both of these facts indicate that the side of the system facing us is more ionized than the far side of η_A's wind. Figs. 7 and 8 show that this is true only if η_B, and hence apastron, is on the observer's side of the system for most of the binary orbit.

The SIMPLEX results appear to favour a formation scenario for the He I lines that is more-or-less consistent with that proposed by e.g. Nielsen et al. (2007), Damineli et al. (2008a), with some modifications. In the following, we consider the Case A simulation results, which most likely represent η_A's current mass-loss rate (M13). The simulations clearly show that with apastron on the observer's side of the system, η_B ionizes portions of the WWIR and pre-shock η_A wind flowing towards the observer. Thus, for most of the orbit, the He I emission lines would form mostly in the blueshifted part of η_A's wind, consistent with the observations. The double, and sometimes multiple, peak profiles observed in He I emission are consistent with emission arising from spatially separated regions in the WWIR. The two ionized dense arms of post-shock η_A wind (Figs. 7 and 8) are very likely the sources of these emission peaks. The broader general component of the He I emission likely arises in both the central η_A wind (due to ionization by η_A itself) and the larger ionization zone within the pre-shock η_A wind located near the WWIR apex.

The observed He I absorption is also blueshifted over η Car's entire spectroscopic cycle, but is relatively weak around apastron (Nielsen et al. 2007). Based on our modelling, this is consistent with the idea that the absorption arises in the ionized pre-shock primary wind located near the WWIR apex, and the ionized portions of the WWIR (specifically, the dense post-shock η_A wind). The gas velocities in these two regions, which are approximately equal to the terminal velocity of η_A's wind, are consistent with the ob-

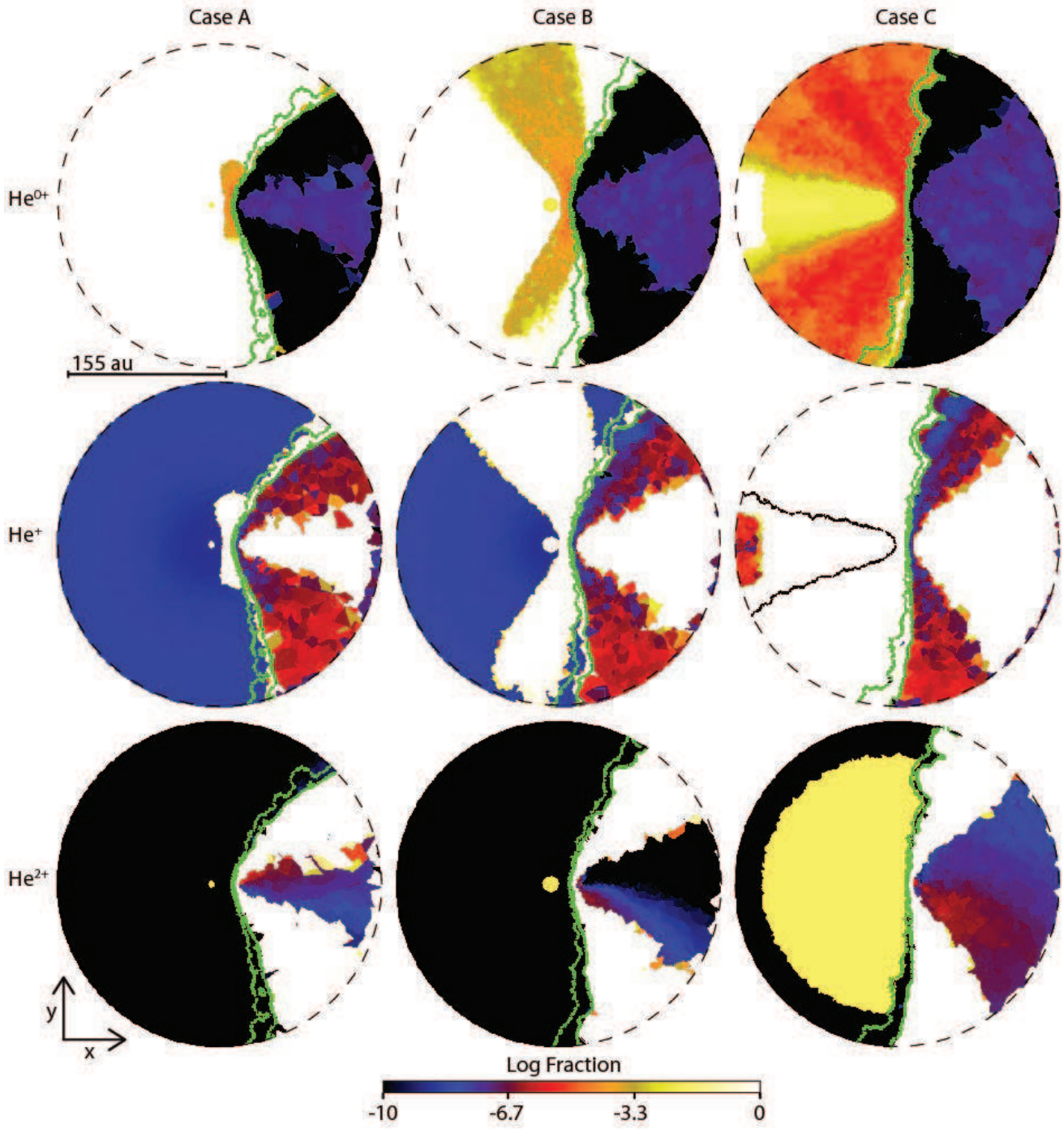

Figure 7. Slices in the orbital plane through the 3D SIMPLEX simulation volume for the three different assumed $\dot{M}_{\eta_A}$ (columns, left to right). Rows show, from top to bottom, the computed fractions of He^{0+}, He^{+}, and He^{2+} (log scale). The circular ionization structure around η_A (i.e. the yellow circular areas in the He^{0+} and He^{2+} rows) is the region where we have set He to He^{+} in the pre-shock primary wind (see Section 2.3.1). The black contour in the right-hand panel of the middle row (Case C, He^{+}) marks the location of the He^{+} ionization front when the ionization structure of η_A's inner wind is excluded in the calculations.

served velocity of the P Cygni absorption in the He I lines (~ -300 to -600 km s^{-1}). Which region dominates the He I absorption in line of sight is uncertain at this point, but the much denser (by at least an order of magnitude) WWIR likely dominates, especially if one considers sight lines that are nearly parallel to and intersecting the WWIR surface (which is likely the case since the binary is inclined by $\sim 45°$ away from the observer; see Madura et al. 2012, 2013). Thus, contrary to the assumption by Nielsen et al. (2007), the observed He I absorption is very likely dominated by material in the post-shock η_A wind, rather than in the pre-shock η_A wind. This is the scenario favoured by Damineli et al. (2008a).

Another important difference between our simulation results and simpler models for η Car's He ionization zones (e.g. Martin et al. 2006; Humphreys, Davidson & Koppelman 2008;

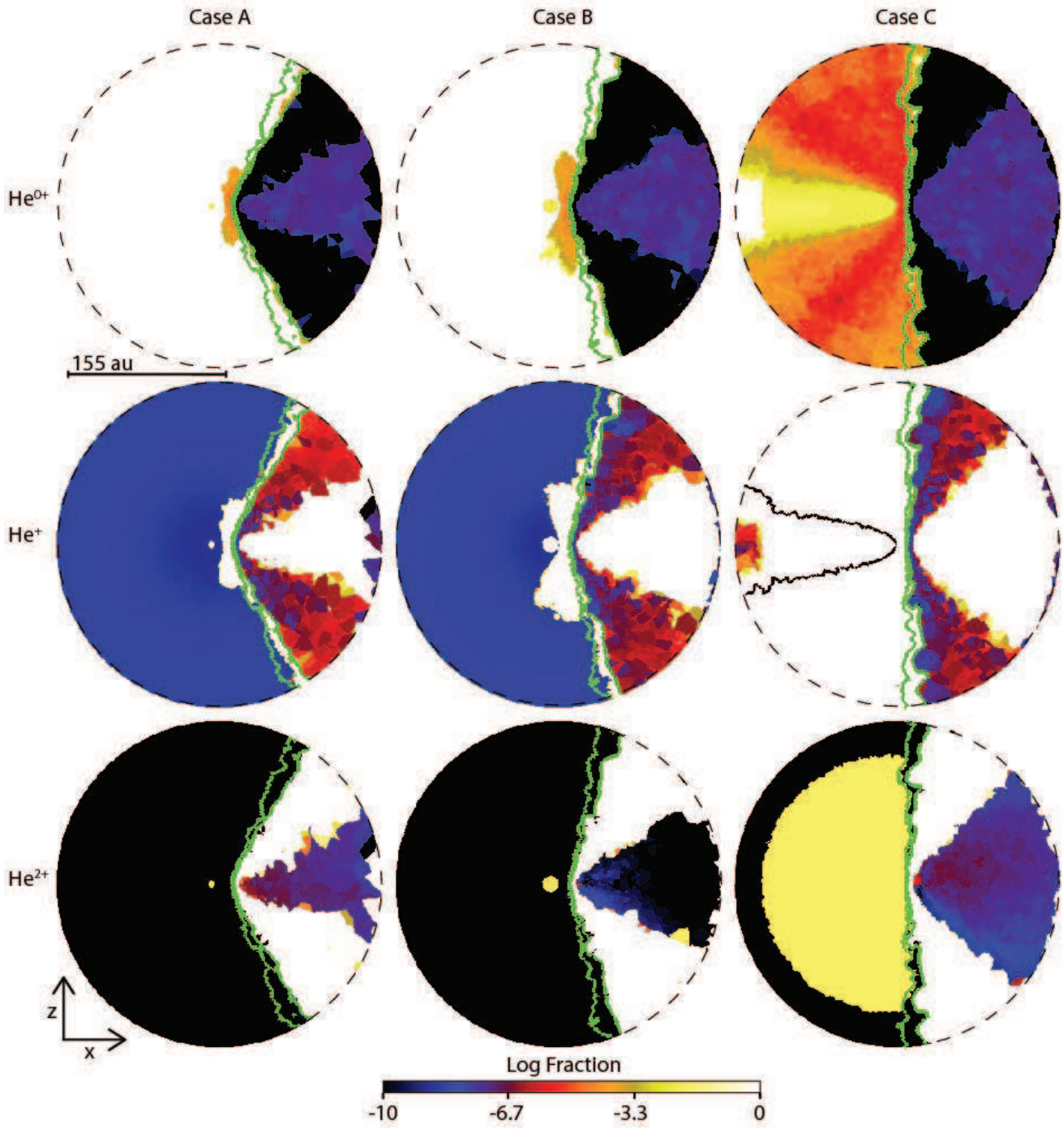

Figure 8. Same as Fig. 7, but for slices centred in the *xz* plane.

Mehner et al. 2012) is the detailed ionization structure of the gas in the pre-shock η_A wind that borders the WWIR. This is due mainly to the complex structure of the WWIR, which in toy models is too simplistic. The WWIR consists of a region of hot, compressed (by roughly a factor of 4) post-shock η_B wind separated by a CD from a thin region of very high density, colder ($T \sim 10^4$ K) post-shock primary wind. The dense, turbulent post-shock η_A wind absorbs most of η_B's He^{0+}-ionizing photons and greatly affects the ionization structure of η_A's pre-shock wind. Detailed examination of Figs. 7 and 8 shows that with the exception of a $r \sim 75$–80 au region about the WWIR apex, the He^+ ionization front due to η_B penetrates only approximately half way into the post-shock η_A wind region. Only in the region near the WWIR apex does η_B singly-ionize He in η_A's pre-shock wind. At larger distances from η_A along the walls of the WWIR, He remains neutral in the pre-shock η_A wind. Thus, simple models like that shown in fig. 12 of Humphreys, Davidson & Koppelman 2008 and fig. 5a of Mehner et al. 2012 are only partially cor-

rect[2], and very dependent upon scalelength (Martin et al. 2006; Humphreys, Davidson & Koppelman 2008 and Mehner et al. 2012 show only a small region near the stars at apastron). The He^+ region around the WWIR apex is also thinner and more geometrically similar to the WWIR in such models than we find in our simulations. The He^+ region in the pre-shock η_A wind in our simulations is more similar to fig. 5b of Mehner et al. (2012), but with the wings of He^+ not bending back farther than the location of η_A.

Mehner et al. (2012) used their fig. 5 to illustrate their interpretation for why the strength of the He I P Cygni absorption observed in η Car has been gradually increasing since 1998, with a sudden absorption increase after the 2009 periastron event (Groh & Damineli 2004; Mehner et al. 2010, 2012). Mehner et al. (2012) attribute the observed increase in absorption, and other changes, to a gradual decrease of $\dot{M}_{\eta_A}$ by a factor of ∼2–3 between 1999 and 2010. They suggest that a drop in $\dot{M}_{\eta_A}$ would change the He ionization structure of η_A's pre-shock wind, as depicted in their fig. 5. Mehner et al. (2012) suggest that the enlarging of the He^+ zone in η_A's pre-shock wind with decreasing $\dot{M}_{\eta_A}$ would lead to more He I absorption in line of sight.

Our SIMPLEX simulations show that, in the orbital plane, the behaviour of the He^+ ionization zone in η_A's pre-shock wind with decreasing $\dot{M}_{\eta_A}$, as suggested by Mehner et al. (2012), is partially correct. We find that a decrease in $\dot{M}_{\eta_A}$ does enlarge the He^+ zone in the pre-shock η_A wind. Moving from Case A to Case B, two large 'wings' of He^+ develop in the pre-shock η_A wind that bend backward around η_A. The post-shock η_A wind also becomes more ionized and contains more He^+ out to larger radii from η_A. However, the He^+ wings in the pre-shock η_A wind do not continuously border the WWIR at all radii in Case B. Near the outer edges of the simulation in the orbital plane, there are clear gaps between the pre-shock η_A He^+ zone and the WWIR. In these small regions, He remains neutral. Moreover, changes to the He ionization structure with decreasing $\dot{M}_{\eta_A}$ are confined mostly to the orbital plane when moving from Case A to Case B. The Case B simulation shows that the He^+ ionization zone in the *xz* plane is much smaller and remains concentrated near the WWIR apex, with no large He^+ wings extending back behind η_A. Decreasing $\dot{M}_{\eta_A}$ even more from Case B to Case C results in η_B ionizing He throughout the entire simulation domain. As discussed above and in M13, such a low $\dot{M}_{\eta_A}$ appears to be ruled out by numerous observations.

Based on these results, a small-to-moderate decrease (by no more than a factor of 2) in $\dot{M}_{\eta_A}$, similar to the simple model suggested by Mehner et al. (2012), may help explain the observed increase in He I absorption. The key question is, how much He I emission and absorption does an ionization structure like that in Case B produce in line of sight? One might expect such a large change in the He^+ zone within η_A's pre-shock wind to result in a significant detectable change in the amounts of He I and He II emission. An increase in the amount of He^+ near the WWIR that is available to be ionized by very soft X-rays generated in the post-shock η_A gas as it radiatively cools should lead to increased He II λ4686 emission throughout the binary orbit. Significant changes in the amount of He II λ4686 emission during the broad part of η Car's orbit are not observed though, and the behaviour of the λ4686 emission during recent spectroscopic events has been amazingly similar (Teodoro et al., in preparation). The lack of any major changes in the observed λ4686 emission may imply that the amount of He^+ available in the pre-shock η_A wind at phases around apastron is not the key factor in determining the amount of λ4686 emission. Rather, there may be a limited number of suitable photons generated in the WWIR that can produce λ4686 emission in the available He^+ zone. As such, we suggest that the small amount of He II λ4686 emission that is observed across η Car's entire orbital cycle originates in the He^+ zone in η_A's pre-shock wind that surrounds the apex of the WWIR, with the high-energy photons required for such emission originating in the nearby post-shock η_A wind.

However, the above scenario does not remedy the problem of why there has been no observed increase in the amount of He I emission. If the efficiency for creating He II λ4686 emission around apastron is low, even though the amount of He^+ in η_A's wind is high, one would expect increased He I emission. A possible explanation for the lack of increased emission is that the larger volume of ionized post-shock η_A wind is absorbing the He^{0+} photons generated in the larger pre-shock η_A He^+ zone. The details of how the amounts of emission and absorption in line of sight change as the WWIR opening angle increases (due to the decreased $\dot{M}_{\eta_A}$ and altered wind momentum ratio) are poorly understood at this time, and it is unclear whether any decrease in $\dot{M}_{\eta_A}$ was gradual (between ∼1998 and now) or sudden (during/after the 2009 periastron event). More detailed observations and theoretical models are needed to better understand the nature of η Car's He I lines.

Finally, based on our results, we speculate on a possible solution to an interesting problem concerning He^{0+} in η Car, namely, why there are no observed signatures of the broad He I emission lines in spectra obtained before 1944 if η Car is a binary containing a hot companion star (for details, see Humphreys, Davidson & Koppelman 2008). This is seen as a problem because it is assumed that η_B, if it exists and is a hot, massive star, should always ionize a significant volume of η_A's pre-shock stellar wind, leading to detectable He I emission. Such emission is only marginally present (at best) in early spectra obtained between η Car's second eruption in the 1890s and 1944. Humphreys, Davidson & Koppelman (2008) argue that, even if $\dot{M}_{\eta_A}$ was larger in the past, η_B would still have ionized η_A's pre-shock wind, which should lead to He I emission in the early spectra.

As shown in Section 3 and discussed above, the results of detailed 3D hydrodynamical and RT simulations can differ substantially from the expectations of a simple model like that in fig. 12 of Humphreys, Davidson & Koppelman (2008). Our Case A simulations show that η_B's He^{0+}-ionizing photons only moderately penetrate the dense post-shock η_A wind at radii $\gtrsim$75 au from the star, and that only the pre-shock wind in the inner ∼75 au around the WWIR apex is He^+. We also see from our Case B and Case C results that a factor of 2–4 change in $\dot{M}_{\eta_A}$ can lead to major changes in the ionization structure of He in η_A's pre-shock wind. Therefore, we suggest that the reason broad He I lines were not observed in spectra of η Car before 1944 is because $\dot{M}_{\eta_A}$ was larger then (by at least a factor of 2–4, or more) than it is now.

While SIMPLEX results using 3D SPH simulations that employ a higher $\dot{M}_{\eta_A}$ are needed to test this hypothesis, we can speculate what the resulting He-ionization structure would look like in such a situation where $\dot{M}_{\eta_A}$ is roughly a factor of 2 or more larger than its present value. Given the results in Figs. 7 and 8, the post-shock η_A wind was probably so dense it absorbed nearly all incoming He^{0+}-ionizing photons from η_B, preventing ionization of the He^{0+} in η_A's pre-shock wind. There was also probably much less He^+ in the post-shock η_A wind since any such He^+ that formed there would likely quickly recombine due to the extremely high densities in that region. There would moreover be little-to-no intrinsic He I emission from η_A itself, since the inner He^+ zone in its pre-shock

[2] They appear to neglect the post-shock η_A wind region and CD.

wind would extend to $r < 2.5$ au[3] from the star. Because the wind momentum ratio would be dominated by η_A's much denser wind, the opening angle of the WWIR would be much smaller, bringing the two arms of hot, post-shock η_B wind closer together. Conceivably, the two arms could be so close they practically overlap, in which case the wind of η_B would be dominated by collisionally-ionized He^{2+}, with perhaps only a very narrow region of He^+ extending behind η_B (caused by photoionization of the remaining receding pre-shock wind). With practically no He^+ present in the inner η Car system, there would be no, or only marginal, He I emission detectable, thus explaining the early spectral observations.

An enhanced $\dot{M}_{\eta_A}$ between the 1890s and 1944 is quite possible, and even likely, since η Car had just experienced its second eruption, wherein it ejected ~0.1 $M_\odot$ and formed the 'Little Homunculus' (Ishibashi et al. 2003; Smith 2005). The dense, slow-moving near-equatorial circumstellar ejecta known as the Weigelt blobs (Weigelt & Ebersberger 1986) were also ejected around this time. It is therefore not unreasonable to suggest that the LBV primary had a larger mass-loss rate following these events, which slowly decreased to a more stable and 'normal' value by ~1944. During this period of higher $\dot{M}_{\eta_A}$, the ionizing flux from η_B was probably more confined and could not penetrate the denser WWIR, leading to the absence of any significant He I emission.

5 SUMMARY AND CONCLUSIONS

We investigated the effects of the hot secondary star's ionizing flux on η Car's inner winds and WWIR, focusing on the ionization structure of helium during the spectroscopic high state (i.e. orbital phases around apastron). We used SIMPLEX to post-process 3D SPH simulation output of the innermost region of the η Car system. Compared to our previous work, we implemented several changes and improvements in the RT simulations. Assigning to the SIMPLEX cells the SPH number density, instead of a Voronoi cell-volume approach, results in density distributions in SIMPLEX that are less affected by local differences in the SPH particle distribution. Sampling the η_B blackbody spectrum with three frequency bins and the use of DCT also lead to more physically realistic results, and hence more precise ionization fractions and front locations for H and He. Below we summarize our most important results.

1. The inclusion of the He^+ ionization volumes around the primary star η_A does not produce relevant differences in the final ionization results for simulations with high $\dot{M}_{\eta_A}$ (Cases A and B). The exception is Case C, wherein $\dot{M}_{\eta_A}$ is so low η_A fully ionizes H everywhere, and singly-ionizes He out to a radius of ~120 au. η_B is thus able to completely singly-ionize He throughout the entire computation domain in Case C. We are therefore able to rule out Case C as a possible current value for $\dot{M}_{\eta_A}$.
2. The SIMPLEX results show that η_B's He^{0+}-ionizing photons are able to penetrate the WWIR and reach the unperturbed η_A wind to varying degrees, depending on the value of $\dot{M}_{\eta_A}$. The geometry and extent of the He-ionization structures in the pre- and post-shock η_A wind depend strongly on $\dot{M}_{\eta_A}$.
3. He^{0+} is confined to the pre- and post-shock η_A wind for higher $\dot{M}_{\eta_A}$. The volume of He^+ in the pre- and post-shock η_A wind increases as $\dot{M}_{\eta_A}$ decreases. As expected, η_B singly-ionizes He in its pre-shock wind. He^{2+} is produced, through collisional ionization, in the hot post-shock η_B wind.
4. The different extents of the He-ionization fronts into η_A's wind in both the orbital and *xz* planes might be caused by differences in the density and temperature state of the WWIR. Small holes or regions of lower density in the unstable post-shock η_A wind region may also allow He^{0+}-ionizing photons to penetrate the WWIR and ionize different portions of η_A's pre-shock wind.
5. The location of the He^+ region in our simulations provides further support for binary orientations in which apastron is on our side of the system (Damineli et al. 2008a; Okazaki et al. 2008; Parkin et al. 2009, 2011; Madura et al. 2012, 2013). The SIMPLEX results favour a formation scenario for the He I lines that is mostly consistent with that proposed by Damineli et al. (2008a).
6. Based on our results, a small-to-moderate decrease (by no more than a factor of 2) in $\dot{M}_{\eta_A}$, similar to the simple model suggested by Mehner et al. (2012), may help explain the observed increase in He I absorption in η Car. However, numerous questions remain regarding this scenario, such as why such a decrease in $\dot{M}_{\eta_A}$ does not also lead to an increase in He I emission.
7. We suggest that the small amount of He II λ4686 emission observed across η Car's entire orbital cycle originates in the He^+ zone in η_A's pre-shock wind that surrounds the apex of the WWIR, with the high-energy photons required for such emission originating in the nearby post-shock η_A wind.
8. Finally, we suggest that broad He I lines were not observed in spectra of η Car between its 1890s eruption and 1944 (Humphreys, Davidson & Koppelman 2008) because $\dot{M}_{\eta_A}$ was larger then (by at least a factor of 2–4, maybe more) than it is now. During this period of higher $\dot{M}_{\eta_A}$, the ionizing flux from η_B was probably more confined and could not penetrate the denser WWIR, leading to the absence of any significant He I emission.

Our investigation of the He-ionization structure of η Car's inner winds and WWIR helps constrain not only $\dot{M}_{\eta_A}$, but also the nature of the unseen companion η_B. We have shown that our results help explain, and are in qualitative agreement with, available observations of η Car's He I and He II lines. In future work, we plan to use these simulations to generate synthetic spectra for comparison to observational data in order to help place tighter constraints on the binary orientation, $\dot{M}_{\eta_A}$, and η_B's luminosity and temperature. Future improvements to SIMPLEX will allow us to use specific spectral energy distributions for η_B generated from detailed spectroscopic modelling with CMFGEN. These results, together with the ionization structure of He during the spectroscopic low state around periastron (investigated in a subsequent paper), will help us better understand the numerous observed spectral features that arise in the inner ~150 au of the system. Our numerical work also sets the stage for future efforts to couple SIMPLEX with modern 3D SPH and grid-based hydrodynamics codes for even more physically realistic 3D time-dependent radiation-hydrodynamics simulations of η Car and other colliding wind binaries.

ACKNOWLEDGEMENTS

We thank Jose Groh, Noel Richardson, and Vincent Icke for useful discussions and comments. TIM is supported by an appointment to the NASA Postdoctoral Program at the Goddard Space Flight Center, administered by Oak Ridge Associated Universities through a contract with NASA. Support for TRG was through programs #12013, 12508, 12750, 13054, and 13395, provided by NASA through a grant from the Space Telescope Science Institute,

[3] The exact value requires a specific assumed value of $\dot{M}_{\eta_A}$ and detailed spectroscopic modelling with e.g. CMFGEN.

which is operated by the Association of Universities for Research in Astronomy, Inc., under NASA contract NAS 5-26555.

REFERENCES

Agertz O. et al., 2007, MNRAS, 380, 963
Clementel N., Madura T. I., Kruip C. J. H., Icke V., Gull T. R., 2014, MNRAS, 443, 2475 (C14)
Corcoran M. F., 2005, AJ, 129, 2018
Corcoran M. F., Hamaguchi K., Pittard J. M., Russell C. M. P., Owocki S. P., Parkin E. R., Okazaki A., 2010, ApJ, 725, 1528
Damineli A., 1996, ApJ, 460, L49
Damineli A., Conti P. S., Lopes D. F., 1997, New A, 2, 107
Damineli A. et al., 2008a, MNRAS, 386, 2330
Damineli A. et al., 2008b, MNRAS, 384, 1649
Davidson K., Humphreys R. M., 1997, ARA&A, 35, 1
Ferland G. J., Korista K. T., Verner D. A., Ferguson J. W., Kingdon J. B., Verner E. M., 1998, PASP, 110, 761
Friedrich M. M., Mellema G., Iliev I. T., Shapiro P. R., 2012, MNRAS, 421, 2232
Gayley K. G., Owocki S. P., Cranmer S. R., 1997, ApJ, 475, 786
Gomez H. L., Vlahakis C., Stretch C. M., Dunne L., Eales S. A., Beelen A., Gomez E. L., Edmunds M. G., 2010, MNRAS, 401, L48
Groh J. H., Damineli A., 2004, IBVS, 5492, 1
Groh J. H., Hillier D. J., Madura T. I., Weigelt G., 2012a, MNRAS, 423, 1623
Groh J. H., Madura T. I., Hillier D. J., Kruip C. J. H., Weigelt G., 2012b, ApJ, 759, L2
Groh J. H., Madura T. I., Owocki S. P., Hillier D. J., Weigelt G., 2010a, ApJ, 716, L223
Groh J. H. et al., 2010b, A&A, 517, A9
Gull T. R., Madura T. I., Groh J. H., Corcoran M. F., 2011, ApJ, 743, L3
Gull T. R. et al., 2009, MNRAS, 396, 1308
Hamaguchi K. et al., 2007, ApJ, 663, 522
Hamaguchi K. et al., 2014, ApJ, 784, 125
Henley D. B., Corcoran M. F., Pittard J. M., Stevens I. R., Hamaguchi K., Gull T. R., 2008, ApJ, 680, 705
Hillier D. J., Davidson K., Ishibashi K., Gull T., 2001, ApJ, 553, 837
Hillier D. J. et al., 2006, ApJ, 642, 1098
Humphreys R. M., Davidson K., Koppelman M., 2008, AJ, 135, 1249
Ishibashi K. et al., 2003, AJ, 125, 3222
Kruip C., 2011, PhD thesis, University of Leiden, Leiden, the Netherlands
Kruip C. J. H., Paardekooper J.-P., Clauwens B. J. F., Icke V., 2010, A&A, 515, A78
Luo D., McCray R., Mac Low M.-M., 1990, ApJ, 362, 267
Madura T. I., 2010, PhD thesis, University of Delaware
Madura T. I., Groh J. H., 2012, ApJ, 746, L18
Madura T. I. et al., 2013, MNRAS, 436, 3820 (M13)
Madura T. I., Gull T. R., Owocki S. P., Groh J. H., Okazaki A. T., Russell C. M. P., 2012, MNRAS, 420, 2064
Martin J. C., Davidson K., Humphreys R. M., Hillier D. J., Ishibashi K., 2006, ApJ, 640, 474
Martins F., Schaerer D., Hillier D. J., 2005, A&A, 436, 1049
Mehner A., Davidson K., Ferland G. J., Humphreys R. M., 2010, ApJ, 710, 729
Mehner A., Davidson K., Humphreys R. M., Ishibashi K., Martin J. C., Ruiz M. T., Walter F. M., 2012, ApJ, 751, 73
Mehner A., Davidson K., Martin J. C., Humphreys R. M., Ishibashi K., Ferland G. J., 2011, ApJ, 740, 80
Mellema G., Iliev I. T., Alvarez M. A., Shapiro P. R., 2006, New A, 11, 374
Monaghan J. J., 1992, ARA&A, 30, 543
Nielsen K. E., Corcoran M. F., Gull T. R., Hillier D. J., Hamaguchi K., Ivarsson S., Lindler D. J., 2007, ApJ, 660, 669
Okazaki A. T., Owocki S. P., Russell C. M. P., Corcoran M. F., 2008, MNRAS, 388, L39
Owocki S., 2007, in Astronomical Society of the Pacific Conference Series, Vol. 367, Massive Stars in Interactive Binaries, St.-Louis N., Moffat A. F. J., eds., p. 233
Paardekooper J.-P., 2010, PhD thesis, Ph. D. thesis, University of Leiden (2010)
Paardekooper J.-P., Kruip C. J. H., Icke V., 2010, A&A, 515, A79
Paardekooper J.-P., Pelupessy F. I., Altay G., Kruip C. J. H., 2011, A&A, 530, A87
Parkin E. R., Pittard J. M., Corcoran M. F., Hamaguchi K., 2011, ApJ, 726, 105
Parkin E. R., Pittard J. M., Corcoran M. F., Hamaguchi K., Stevens I. R., 2009, MNRAS, 394, 1758
Parkin E. R., Sim S. A., 2013, ApJ, 767, 114
Pawlik A. H., Schaye J., 2008, MNRAS, 389, 651
Pittard J. M., 2009, MNRAS, 396, 1743
Pittard J. M., Corcoran M. F., 2002, A&A, 383, 636
Price D. J., 2007, PASA, 24, 159
Price D. J., 2008, Journal of Computational Physics, 227, 10040
Ritzerveld J., Icke V., 2006, Phys. Rev. E, 74, 026704
Ritzerveld N. G. H., 2007, PhD thesis, Leiden Observatory, Leiden University, P.O. Box 9513, 2300 RA Leiden, The Netherlands
Russell C. M. P., 2013, PhD thesis, University of Delaware, Newark, DE, USA
Smith N., 2005, MNRAS, 357, 1330
Smith N., 2006, ApJ, 644, 1151
Smith N., Gehrz R. D., Hinz P. M., Hoffmann W. F., Hora J. L., Mamajek E. E., Meyer M. R., 2003, AJ, 125, 1458
Steffen W. et al., 2014, MNRAS, 442, 3316
Steiner J. E., Damineli A., 2004, ApJ, 612, L133
Stevens I. R., Blondin J. M., Pollock A. M. T., 1992, ApJ, 386, 265
Stevens I. R., Pollock A. M. T., 1994, MNRAS, 269, 226
Teodoro M. et al., 2012, ApJ, 746, 73
Teodoro M., Damineli A., Sharp R. G., Groh J. H., Barbosa C. L., 2008, MNRAS, 387, 564
Teodoro M., Madura T. I., Gull T. R., Corcoran M. F., Hamaguchi K., 2013, ApJ, 773, L16
Townsend R. H. D., 2009, ApJS, 181, 391
Verner E., Bruhweiler F., Gull T., 2005, ApJ, 624, 973
Weigelt G., Ebersberger J., 1986, A&A, 163, L5